https://doi.org/10.1016/j.jcsr.2021.106760

This is the Pre-Published Version.

# A replaceable fuse steel-concrete composite connection: Force transfer mechanism and design considerations

Xiuzhang He[a, c], Ke Ke[a,b *], Lihua Guo[a], Michael CH Yam[d, e], Zhihui Wang[d]

[a] *School of Civil Engineering, Chongqing University, Chongqing, China*

[b] *Key Laboratory of New Technology for Construction of Cities in Mountain Area (Chongqing University), Ministry of Education, Chongqing, China*

[c] *Tongji Architectural Design (Group) Co., Ltd, Shanghai 200092, China*

[d] *Department of Building and Real Estate, The Hong Kong Polytechnic University, Hong Kong, China*

[e] *Chinese National Engineering Research Centre for Steel Construction (Hong Kong Branch), The Hong Kong Polytechnic University, Hong Kong, China*

## Highlights:

The stress distribution and force transfer mechanism of a novel connection was examined.

The force evolution of the individual elements in the connection was clarified.

A simplified beam model for quantifying the shear resistance of the connection plates was established.

The design equations of the moment/shear resistance of the connection were proposed.

# Graphical Abstract

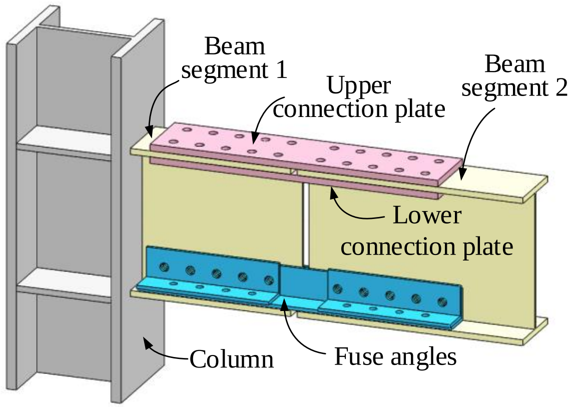

**Configuration of the fuse connection**

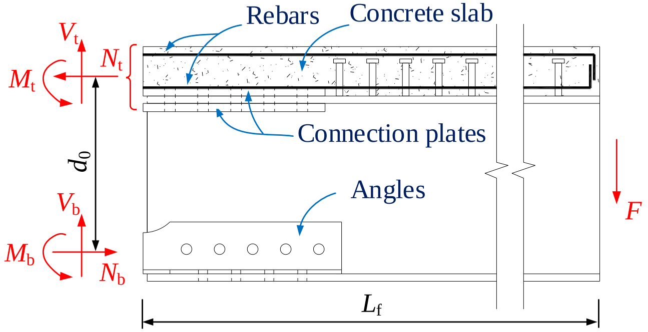

**Free body diagram**

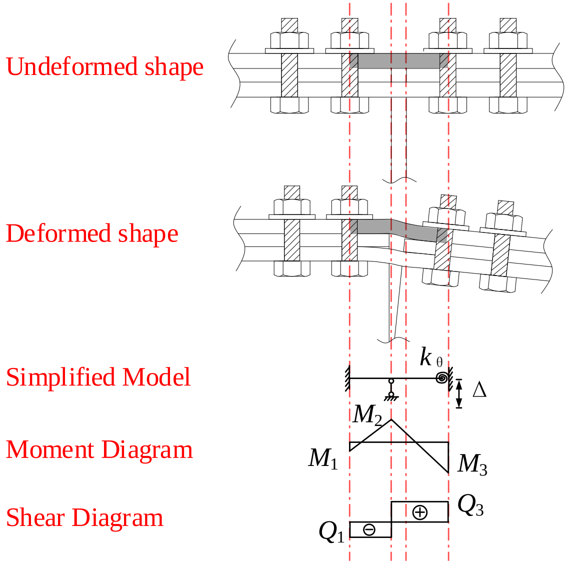

**Shear resistance model**

# A replaceable fuse steel-concrete composite connection: Force transfer mechanism and design considerations

Xiuzhang He[a, c], Ke Ke[a,b *], Lihua Guo[a], Michael CH Yam[d, e], Zhihui Wang[d]

[a] *School of Civil Engineering, Chongqing University, Chongqing, China*

[b] *Key Laboratory of New Technology for Construction of Cities in Mountain Area (Chongqing University), Ministry of Education, Chongqing, China*

[c] *Tongji Architectural Design (Group) Co., Ltd, Shanghai 200092, China*

[d] *Department of Building and Real Estate, The Hong Kong Polytechnic University, Hong Kong, China*

[e] *Chinese National Engineering Research Centre for Steel Construction (Hong Kong Branch), The Hong Kong Polytechnic University, Hong Kong, China*

**Abstract:** This study explored the load-carrying mechanisms of a seismic resistant steel-concrete composite connection with angle fuse elements at the bottom flange. The research was commenced by examining the test results of three full-scale test connections, in particular, the moment/force evolution responses of the connections were studied. Subsequently, detailed finite element (FE) models of the three full-scale test specimens were developed. The predictions by the FE analysis were in good agreement with the test results in terms of the hysteretic responses and the forces of the angles. Following the verification study, the results of the FE analysis were utilised to offer an in-depth insight into the behaviour of the connections, and the force transfer mechanism of the connection was examined. In particular, it was confirmed that the fuse angles could resist the applied moment via axial forces, and the shear resistance was mainly provided by the connection plates at the top flange in the inelastic stage. In addition, an analytical model for quantifying the connection resistance was developed. Design considerations were also proposed to offer design guides for practicing engineers.

**Keywords:** structural fuse; composite connection; finite element model; design considerations

---

* Corresponding author. Email address. kerk.ke@outlook.com

# 1 Introduction

In seismic resistant steel moment-resisting frames, it is expected that plastic hinges are formed at the beam ends to dissipate inelastic energy when structures are subjected to an intense earthquake motion. To ensure formation of plastic hinges at expected locations, properly designed connections (e.g. reduced beam section (RBS) connections [1-3] and connections with reinforced beam ends [4-6]) were proposed and applied in engineering practice. Although these connections can achieve the desirable seismic performances with significant plastic energy dissipation and ductile behaviour, the plastic hinge zones as an integral part of the beam may sustain excessive inelastic deformations in a major earthquake. In this context, practitioners may encounter practical difficulties when attempting to repair the damaged structure.

In order to overcome the drawbacks of conventional ductile energy dissipation connections mentioned above, the research community has carried out numerous studies in the past decades. One simple but feasible solution is to concentrate the inelastic damages to replaceable sacrificial structural elements, whereas the remaining structure responds elastically under an expected deformation range. Therefore, after an earthquake attack, the structural system may resume their normal service by replacing the damaged structural elements. Based on this philosophy, a growing number of innovative replaceable “fuse connections” for moment-resisting frames were proposed and examined. In general, these connections can be divided into three groups based on their locations over the beam span: 1) fuse connections right at the column face [7-10]; 2) fuse connections at a distance away from the column face [11-15], and 3) fuse connections in the mid-span of the beam [16, 17]. As for fuse elements in the connection, the energy dissipation mechanism varies with the specific configuration of the connection, and energy dissipation capability may be provided by carbon metal yielding [11, 18, 19], friction [20-22], and other advanced energy dissipation devices [23, 24].

However, major research efforts on fuse connections mentioned above were dedicated to bare steel connections, whereas the influence of composite flooring systems of a practical structure was sometimes overlooked. Recognising that inelastic deformations are expected to be concentrated in the fuse connection, special caution is needed to avoid severe slab damages [25, 26]. In addition, the composite action between the steel beam and the concrete slab may lead to behaviour change of the fuse connection (e.g. shift of the neutral axis [27, 28] and deterioration of rotation capacity [29]). From the perspective of post-earthquake repair work, the interference of the flooring system could also complicate the replacement operation of the fuse connections. Hence the applicability of existing notions of bare steel fuse connections may need to be revisited, and novel steel-concrete composite fuse connections may be needed. Therefore, the first author and colleagues developed an asymmetric fuse connection recently [30], as schematically shown in Fig. 1. For the proposed connection, the steel beam was interrupted at a distance from the column face. The concrete slab was continuous over the gap between beam segments with an additional strengthening of upper layer reinforcement in the slab over the connection. Two adjacent beam segments were connected by strong connection plates at the top flange, and two angles were arranged at the bottom flange to link the beam segments. Fig. 2 shows the individual components of the fuse connection. Under cyclic loading scenarios, the connection is anticipated to limit damages to steel angles placed at the bottom flange for a wide deformation range without damaging the concrete floor slabs. After an expected earthquake, the connections may recover to operation easily by replacing the damaged steel angles. To confirm the effectiveness of the proposed connection, a test programme was conducted by He et al. [30]. The test results demonstrated that the proposed connection can effectively realise the damage-control behaviour by limiting damages in the replaceable steel angles arranged at the bottom flange of the beam for a reasonable deformation spectrum. Test results also showed that the specimens equipped with replaced steel angles exhibited satisfactory hysteretic performance, and both the initial stiffness and the resistance of the specimens with replaced angles were in good agreement with that of the specimen in the virgin state. More detailed information about the test programme was documented in reference [30].

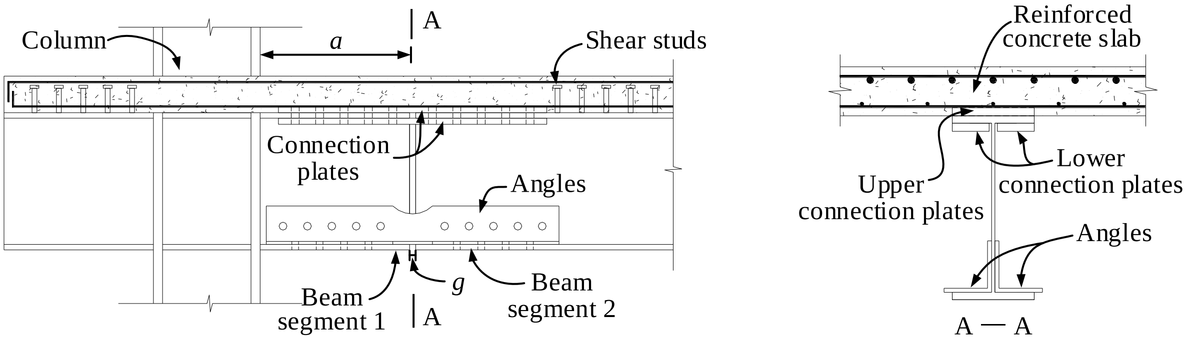

(a) (b)

Fig. 1 Configuration of the composite connection

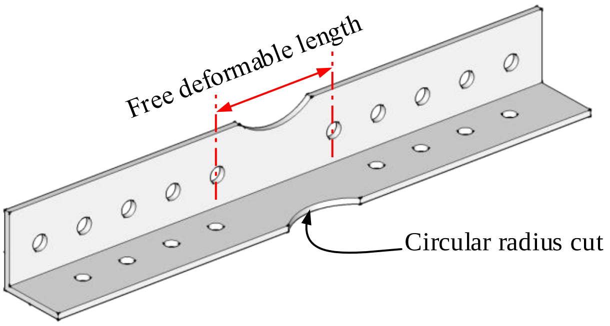

(a) Angle

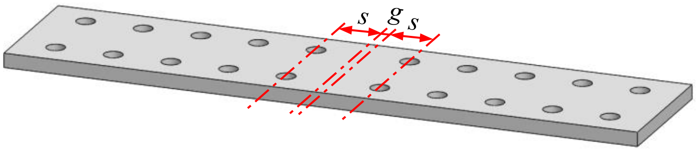

(b) Upper connection plate

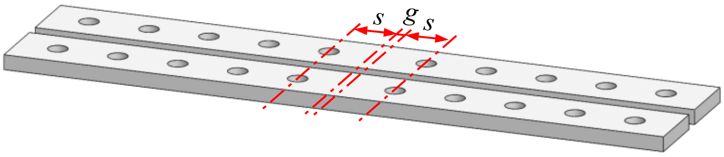

(c) Lower connection plate

Fig. 2 Basic components of the connection

Nevertheless, the previous study focused on the general hysteretic response of the connection (e.g. hysteretic moment versus drift responses) [30]. The practical design guide of the connection and load transfer mechanism has not been thoroughly examined. In light of the above, a research gap concerning the load-carrying behaviour of the composite fuse connection exists, and further studies are needed aiming for the full validation of the connection. As a continuation of the previous study [30], this research attempts to study the detailed force transfer mechanism of the fuse connections. Critical quantities including strain distributions, internal forces and moments of the three test connection specimens [30] under cyclic loading scenarios were presented and discussed. Due to the limitation of instrumentation facilities, only limited test data were captured in the test, whereas detailed and critical mechanical characteristics of the fuse connection (e.g. strain and force distribution evolution in the fuse angles and critical sections) were not fully measured in the test programme. Thus, detailed finite element (FE) models of the test specimens were firstly developed and verified by the test results. Subsequently, essential mechanical characteristics including force and stress distributions of the connections were examined. Based on the experimental results and supplemental findings from the numerical investigation, the force transfer mechanism of the novel fuse connection was clarified. Design considerations of the moment resistance and shear resistance of the connections were also developed, providing a basis for the practical design of the fuse connection.

# 2 Experimental investigation by Chen and colleagues [30]

## *2.1. Test programme*

A total of three full-scale tests on the proposed fuse connection were conducted at the Laboratory of Building Structures at Tongji University, as documented in [30], and the configuration of the test connections is reproduced in Fig. 3 (The slab is not shown in the figures). In the test programme, the research emphasis was given to the influence of the angle configuration (i.e. reduced section angle and end-reinforced angle as shown in Fig. 3) and repairability of the connection. A key parameter, namely the free deformable length, which is defined as the distance between the centrelines of the innermost bolts beside the beam segment gap, was examined in the experimental study (Fig. 2a). As mentioned, in order to limit inelasticity to the fuse angles at large deformations, the plastic moment capacity of the connection was lower than the counterpart of the beam segment. The test rig is reproduced in Fig. 4. Each test subassembly was loaded to a drift of 0.015 rad or 0.02 rad where the connection developed evident inelastic deformations, after which the angles were replaced, and the test specimen was re-tested under cyclic loading scenarios until the specimen experienced severe failure. The test results are designated as P*i*-1 and P*i*-2 for the first and second test respectively for each specimen, where *i* is the specimen number. The information on the test specimens and connection configurations are reproduced in Table 1 and Fig. 3, and the detail was documented in [30]. Note that Fig. 3 only shows the steel elements of the specimens.

Table 1. Details of specimens

| Specimen | Angle configuration | Free deformable length (mm) | Loading drift at first test (rad) | Strengthening plate at web |
|---|---|---|---|---|
| P1 | Reduced section | 210 | 0.015 | Yes |
| P2 | End-reinforced | 130 | 0.015 | No |
| P3 | End-reinforced | 210 | 0.020 | No |

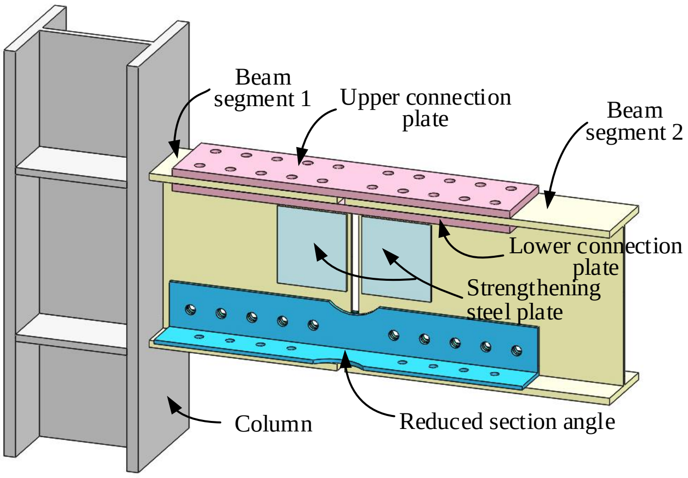

(a) P1

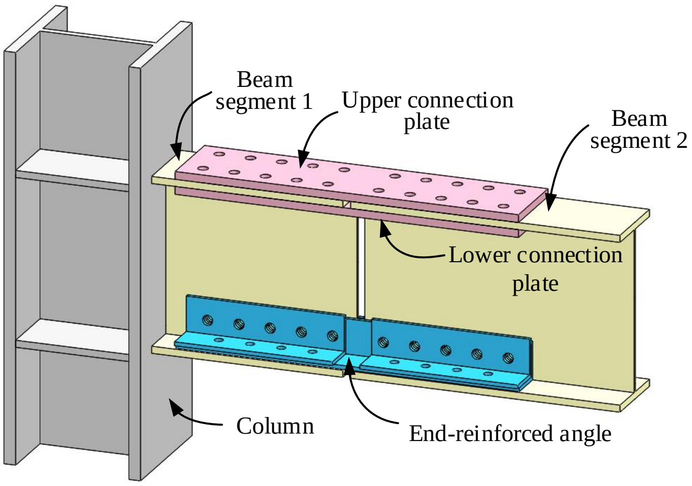

(b) P2

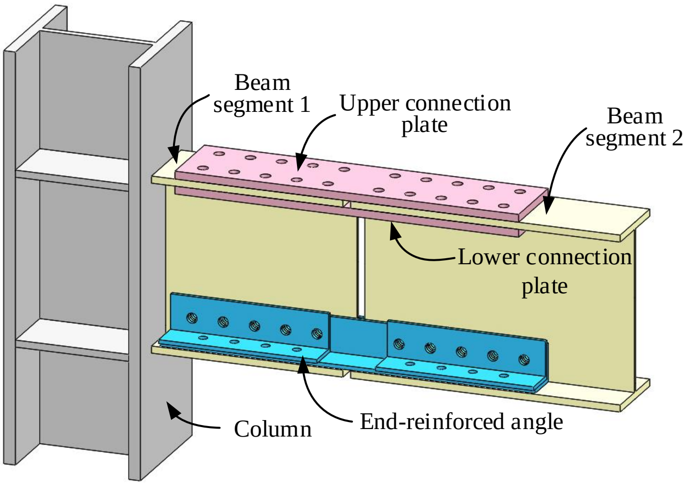

(c) P3

Fig. 3 Specimen geometric configuration

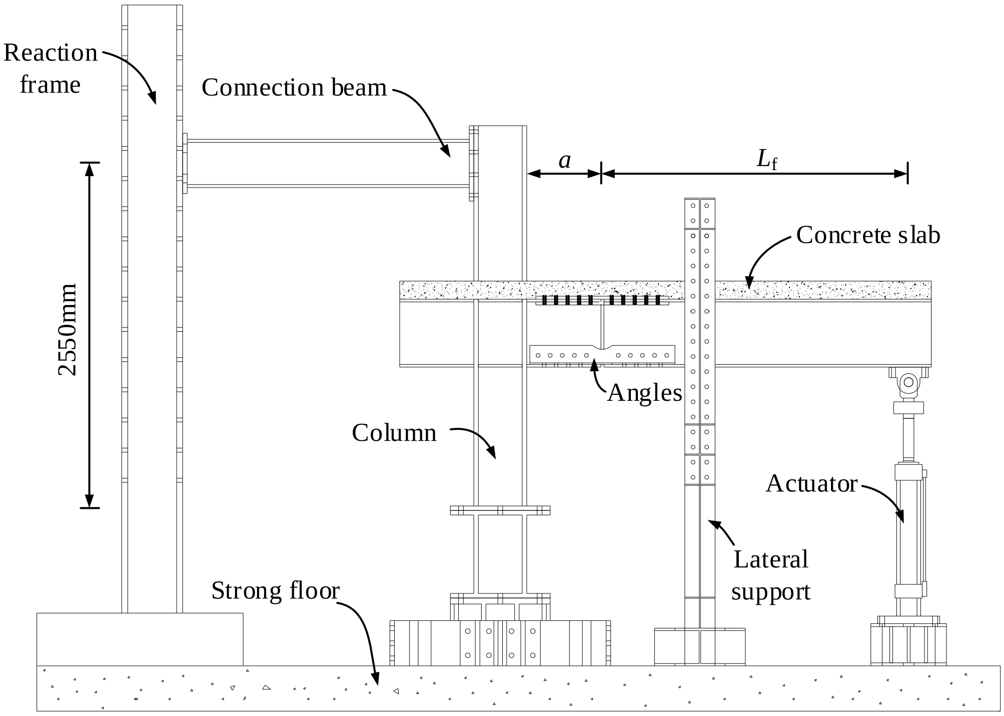

Fig. 4 Test Setup

*2.2. Strain evolution and internal force responses*

In the previous study [30], the hysteretic moment versus deflection responses of the test connections were carefully examined, whereas the strain readings and internal force/moment responses in the connections were not explored. Therefore, the primary objective of the current research is to examine the force transfer mechanism of the connection, and to propose design guidelines for this type of connection.

*2.2.1 Strain readings*

To examine the deformation characteristics of the test connections, strain gauges and displacement transducers were arranged at the critical section, i.e. middle cross-section of the gap in Fig. 5. In particular, strain gauges were mounted at the upper and lower layer rebars embedded in the concrete slab. Displacement transducers were placed at the centreline of the top and bottom flange to measure relative axial deformation of the free deformable length of the connection plates and the angles, respectively. It is worth noting that the equivalent strain of the connection plates or angles was determined by normalising the measured relative axial displacement of the free deformable length, whereas the strain of the rebars was measured by strain gauges. For the three test connections, the strain reading responses in the re-test phases were extracted, and Fig. 6 shows the strain distribution of the critical section at various drift levels.

These results confirmed that the neutral axis of the critical cross-section was close to the centreline of the top flange under both sagging and hogging scenarios. Note that when the test specimens were loaded to a drift beyond 0.02 rad, abnormal strain readings near the centreline of the top flange were observed, which could be possibly due to the looseness of the displacement transducers.

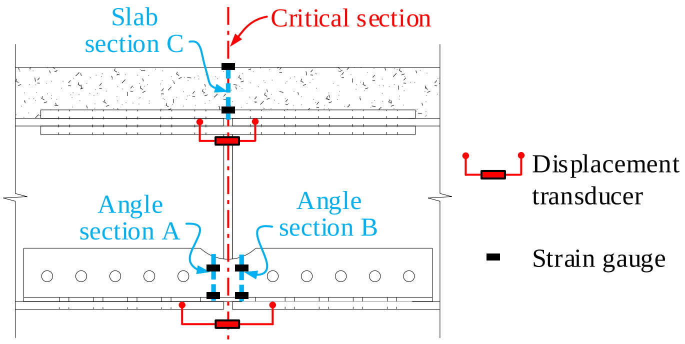

Fig. 5 Instrumentation at the fuse connection.

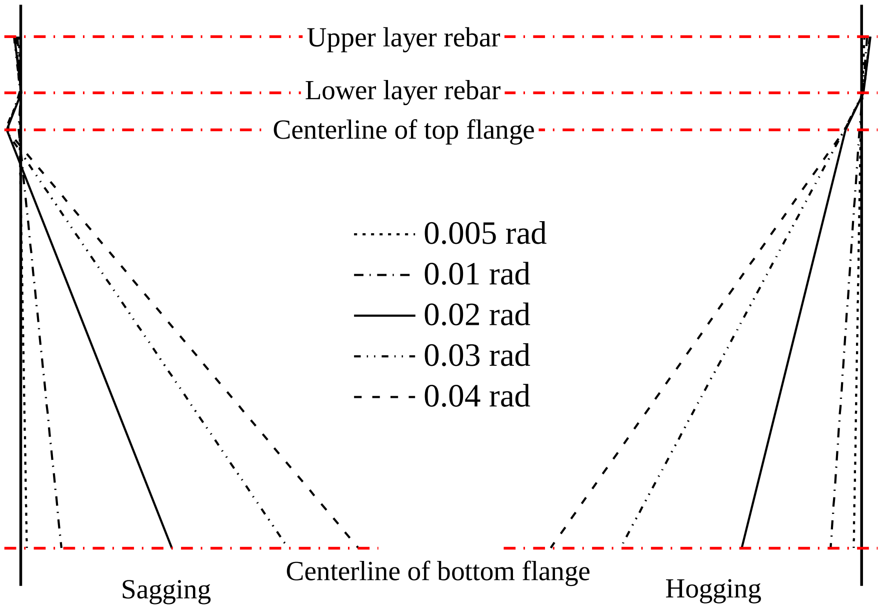

186

187 (a) Specimen P1-2

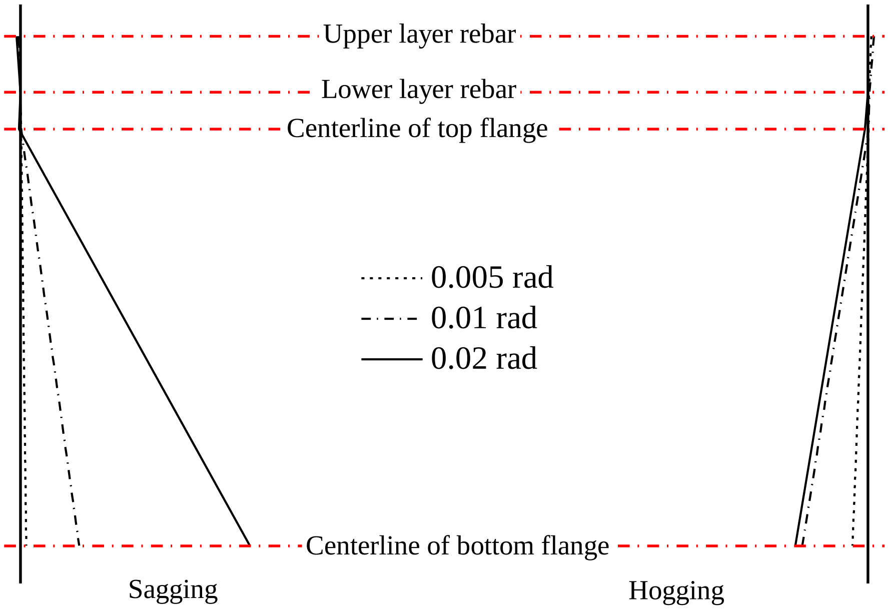

188

189 (b) Specimen P2-2

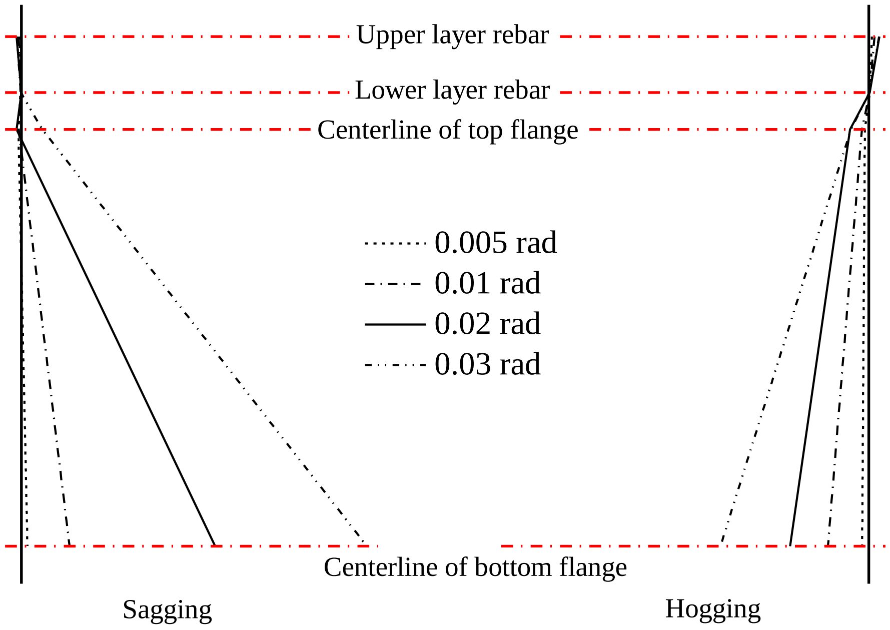

(c) Specimen P3-2

Fig. 6 Strain distribution at the critical section

### *2.2.2 Forces and moment responses*

In the elastic stage, the axial force and moment of one particular section can be calculated by the strain readings at two separate sections based on the plane cross-section assumption. Thus, the axial force and moment of the two-angle sections (i.e. section A and section B in Fig. 5) and a section in the slab (i.e. section C in Fig. 5) can be determined accordingly. The applied load (*F*) by the actuator is plotted against the derived axial forces (*N*) of the angles in the elastic range, as illustrated in Fig. 7. As can be seen, the data points are clustered close to a trend line, implying that the ratio of the applied load to the axial force in the angles is constant. This phenomenon will be discussed in Section 4.1.

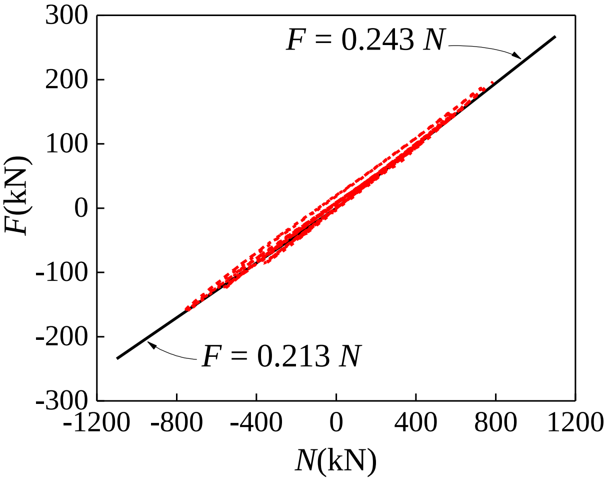

(a) P1-1

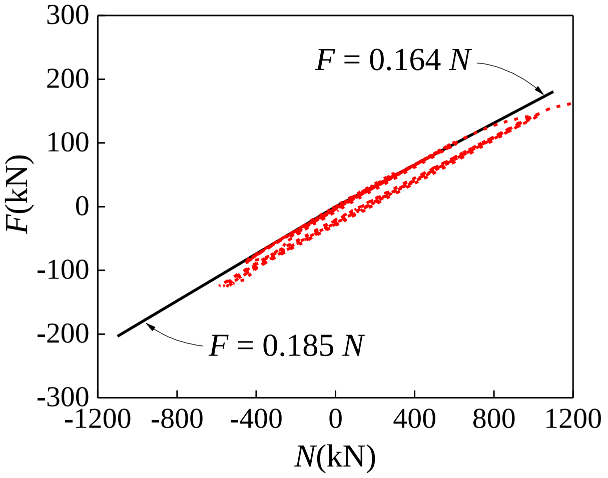

(b) P2-1

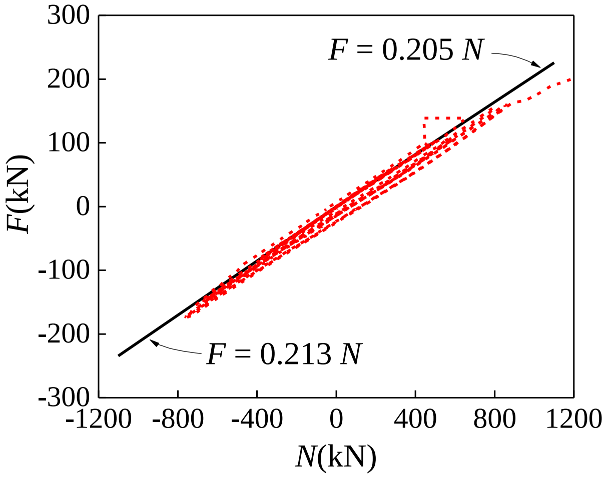

(c) P3-1

Fig. 7 Axial force of angles

Fig. 8 demonstrates the moment responses of the angles at two discrete sections (i.e. Section A and B in Fig. 5) and that of the concrete slab at “section C” when the connections deformed in the generally elastic stage. As shown in the figure, $M$ is the applied moment at the critical section, which was determined by static force equilibrium (i.e. $M = FL_f$, where $L_f$ = distance between the critical section and the load line of the actuator as illustrated in Fig. 4). $M_a$ and $M_c$ are the computed moment of angle section (Section A and Section B) and slab section (Section C), which was derived from strain readings. As can be seen, the slope of $M$ versus $M_c$ confirmed that the concrete slab took only 4%~5% of the total moment at the critical section. Similarly, it can be confirmed that the moment taken by angles at the critical section was much lower than $M$ according to the moment responses at Section A and Section B. In this context, it can be seen that the applied moment at the critical section was mainly resisted by the axial force of angles and concrete slabs.

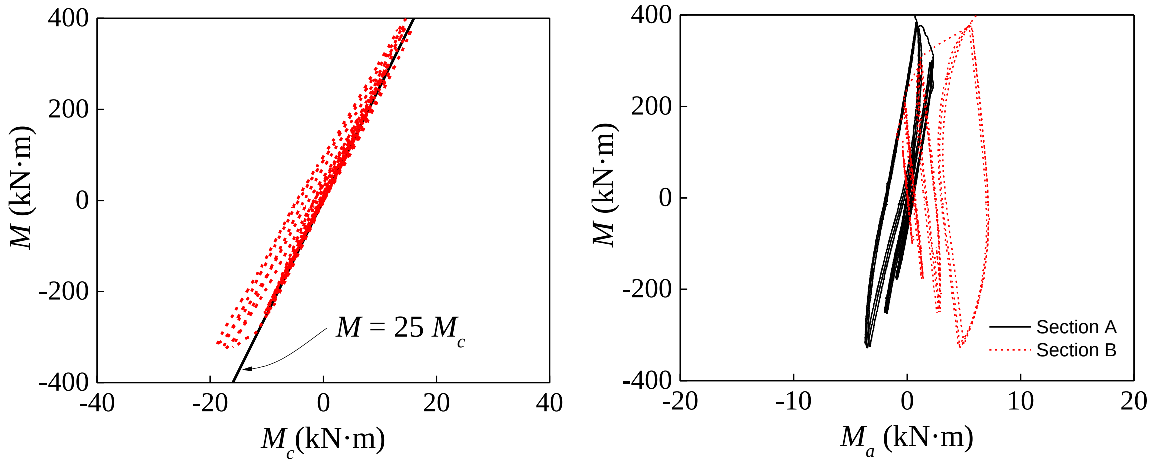

(a) Slab section (b) Angle sections

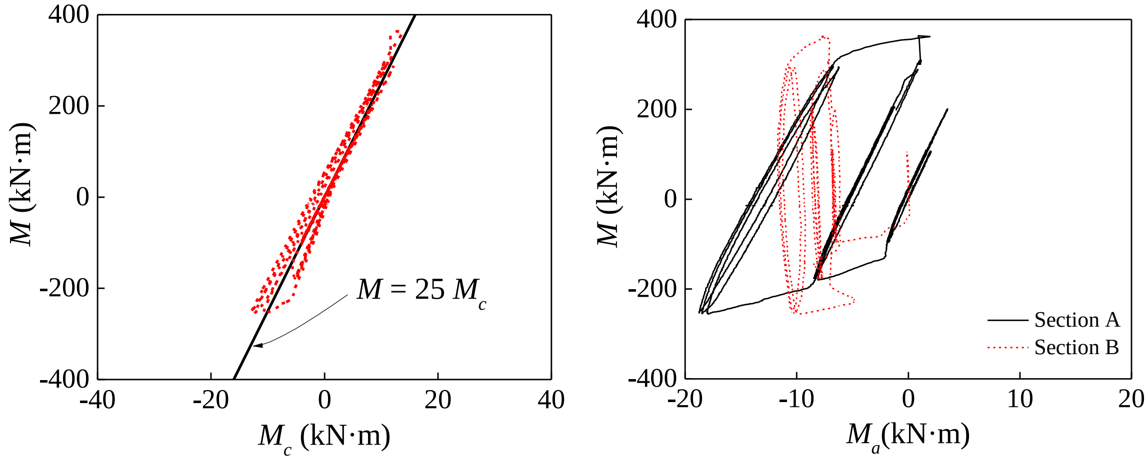

(c) Slab section

(d) Angle sections

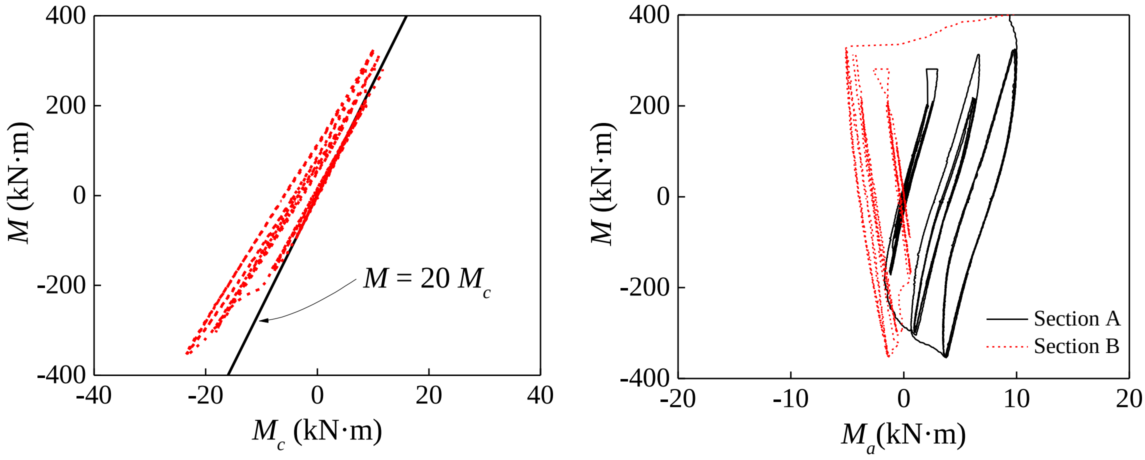

(e) Slab section

(f) Angle sections

Fig. 8 Bending moment at the slab and angles sections

## 3 Numerical investigation

As mentioned, although the full-scale tests offered direct comprehension of the hysteretic behaviour of the novel connection, it was difficult to include sufficient instrumentation to fully collect the force and stress evolutions of the connection components under complicated loading conditions. Thus, nonlinear finite element analysis of the test specimens was conducted to help explain the detailed force transfer behaviour of the connection. Additionally, it has been shown that finite element models were able to accurately predict the behaviour of steel-concrete composite beams, including failure modes, resistance capacity, and the composite action [e.g. see 31-35].

### *3.1 Model description*

Detailed finite element (FE) models of test specimens were created using commercial software LS-DYNA [36], and the overview of a representative FE model is schematically shown in Fig. 9. All the geometry and dimensions of the FE models were identical to that of the test specimens. The column stub, beam segments, angles, bolts, and concrete slab were modelled using eight-node hexahedron elements with constant stress solid element formulation, and rebars in the slab were simulated by truss elements. The connection region applied a refined mesh with an element size of approximately 10 mm, while the rest parts applied a coarse mesh with an element size of approximately 60~80 mm. This resulted in 85000 ~ 90000 solid elements for one specimen. It is worth noting that nodes of the rebar truss elements were coupled with surrounding concrete solid elements as often implemented in the simulation of a reinforcement concrete slab [31,32], and hence the concrete slab and rebars were fully bonded in the modelling, which was a reasonable assumption as no slippage of rebar was detected in the tests.

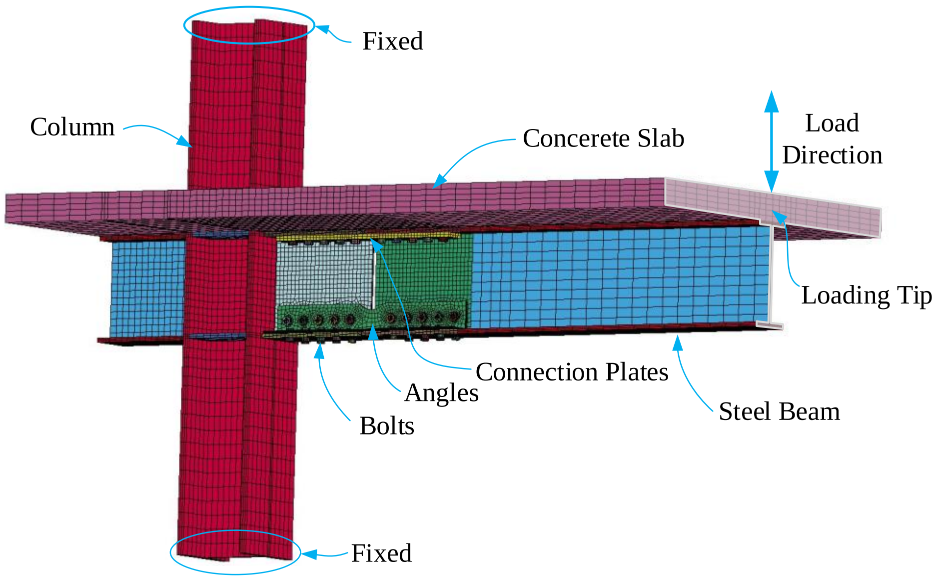

Fig. 9 A representative numerical model (specimen P1)

“Surface-to-surface” contact interactions without penetrations were defined among the interface between separate parts (e.g. bolts, beam segments, connection plates, and angles). The interaction between the bolt head/nut and bolt holes was also simulated. A Coulomb formulation with a friction coefficient of 0.3 was used for all contact surfaces. As no weld failure was detected in the test programme, characteristics of the welds were not simulated in the models, and “merge” strategy was employed to simulate all welds. Moreover, since fully composite beams were designed for the test specimens, shear studs arranged on the top flange of the beam segments were not explicitly modelled. Instead, “Tie” restraint was applied between the outer surface of the top flange and the concrete slab at the shear stud region. The adequacy of the simplification was justified by the test observations as no slippage between the slab and steel beam was observed. The two ends of the column stub were fixed by restraining all translational and rotational displacements, and the cyclic loads were applied at the free end of the composite beam.

A bilinear kinematic hardening law was utilised to reproduce the cyclic response of the steel material based on the measured material characteristics from the coupon tests [30], and a post-yielding stiffness ratio of 0.01 was used. To rationally simulate the behaviour of concrete subjected to cyclic loading conditions, a material model developed by Moharrami and Koutromanos [37], which may be used to reproduce crack opening and closing behaviour of concrete, was employed in the analysis based on the material properties of the concrete samples. Essential parameters of the concrete model are listed in Table 2.

Table 2. Essential parameters of the concrete model

| $E_c$ (MPa) | $v$ | $G$ (MPa) | $K$ (MPa) | $f_c$ (MPa) | $\varepsilon_0$ | $f_0$ (MPa) | $f_t$ (MPa) |
|---|---|---|---|---|---|---|---|
| $2.6\times10^5$ | 0.2 | $1.1\times10^5$ | $1.46\times10^5$ | 27.5 | 0.0025 | 18.3 | 2.93 |

Note: $E_c$ = young's modulus of concrete; $v$= posisson's ratio; $G$ = shear modulus; $K$ = bulk modulus; $f_c$ = compressive strength; $\varepsilon_0$ = strain at peak compressive strength; $f_0$ = the value of initial yield stress; $f_t$ = tensile strength of concrete.

The analyses employed an implicit solver with the quasi-Newton method for nonlinear solution. There are two loading steps: 1) bolt pretension loading with the "dynamic relaxation" option provided in LS-DYNA software and 2) cyclic loading applied with the same displacement protocol as the experimental loading protocol.

### *3.2 Verification of modelling techniques*

#### *3.2.1 Hysteretic force versus drift responses*

Force versus drift responses were extracted from the FE database and compared with the test results, as shown in Fig. 10. In general, the FE predictions are in good agreement with the test responses. It is worth mentioning that since deterioration of material properties and fracture of the steel material were not employed in the modelling, the FE models were not able to capture the strength degradation associated with fracture when the load drift exceeded 0.028 rad. This does not, however, affect the model's ability to capture the stress and force distribution pattern in the connection, which will be elaborated on in later sections.

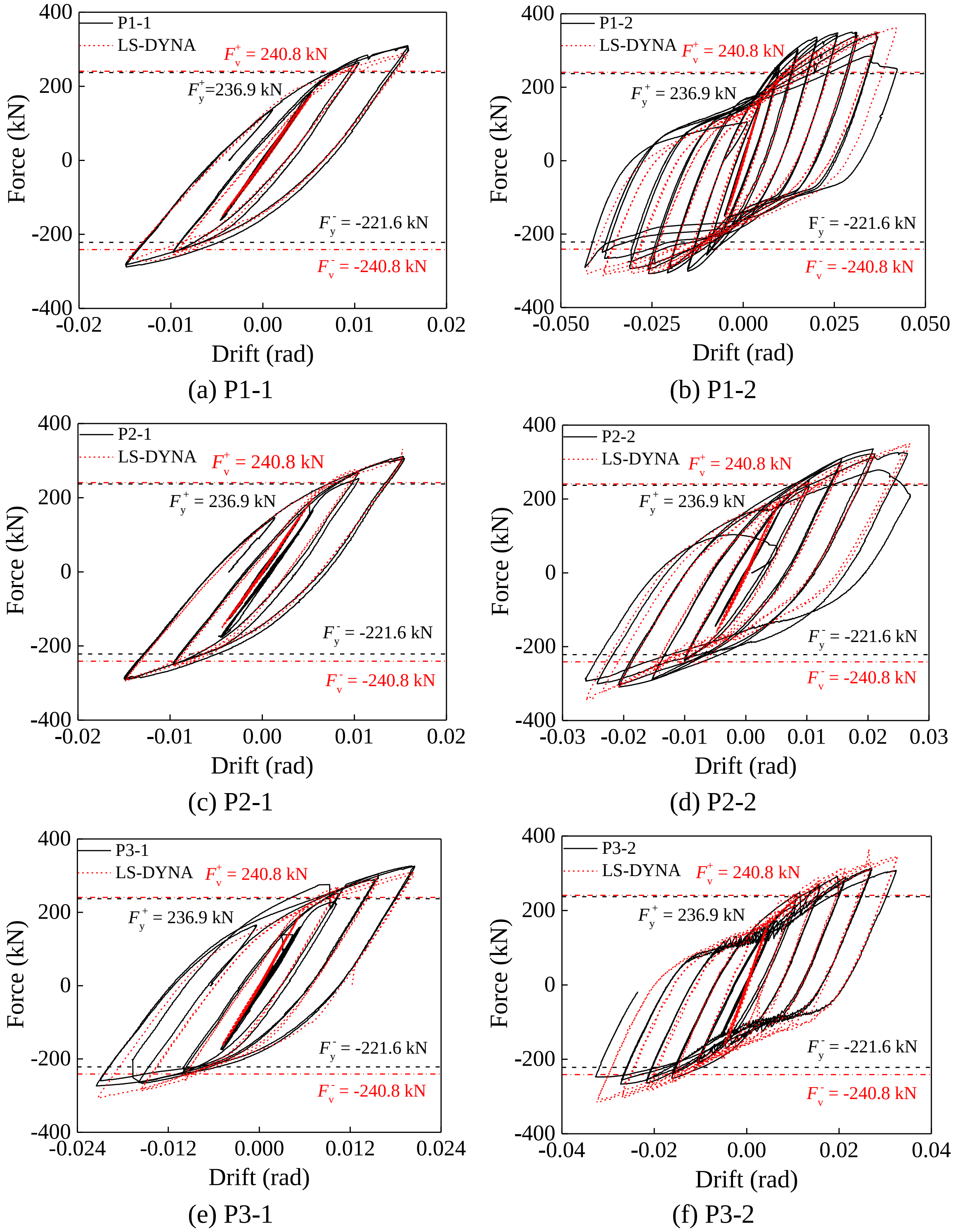

(a) P1-1 (b) P1-2

(c) P2-1 (d) P2-2

(e) P3-1 (f) P3-2

Fig. 10 Load-deformation curves

### *3.2.2 Axial forces in angles*

Fig. 11 compares the resultant axial force of the bottom angles of FE models and that extracted from the test database when specimens responded in the elastic stage (till load cycles below 15 mm corresponding to the drift of 0.0056 rad). As can be seen, the axial force evolution of the angles predicted by FE models was in reasonable agreement with the test results. Note that the FE model did not accurately predict the axial forces of the angles in specimen P2-1. This discrepancy might be attributed to the inaccurate strain readings in the specimen P2-1 that was used to calculate the axial force. Nevertheless, from the perspective of the general trend, these results confirmed the adequacy of the FE models for capturing the mechanical behaviour of the fuse angle in the connections.

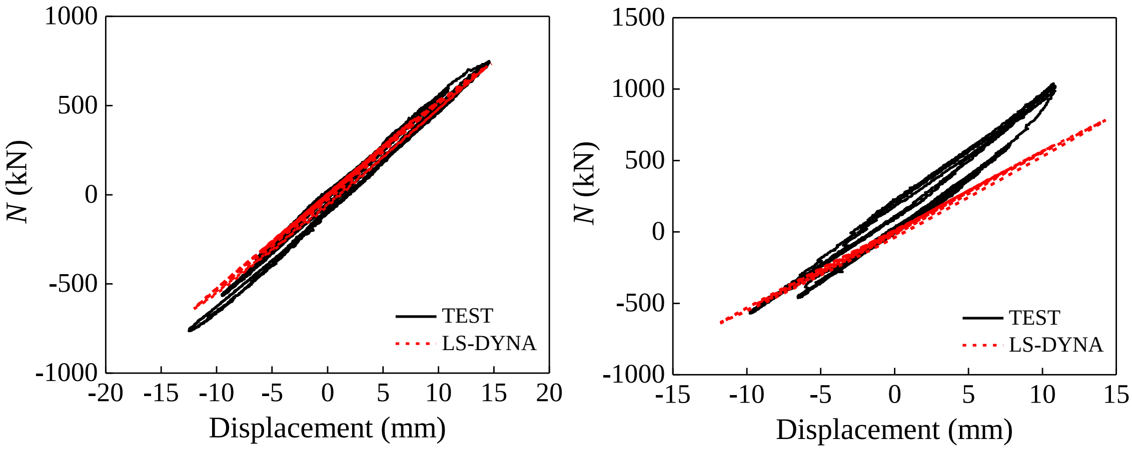

(a) P1-1 (b) P2-1

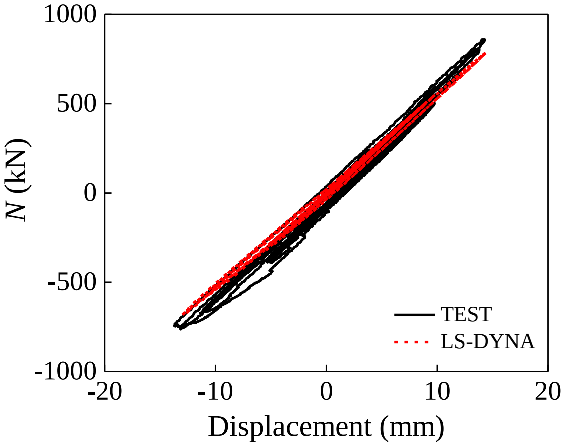

(c) P3-1

Fig. 11 Axial force of angles

### 3.2.3 Force transfer mechanism and comments

The validated FE models facilitated further interpretation of the force transfer mechanism of the connection. Two important facets of the connection behavior were examined in detail: 1) stress distribution in the web panel and 2) shear force distribution at the critical section. These numerical results may contribute to the development of practical design methods of the connection.

As a representative case, Fig. 12 and Fig. 13 demonstrate the von Mises stress contour and principal stress vectors of the web of specimen P3 at the drift of 0.015 rad. As shown in Fig. 12, the stress is significant at the top corner of the web close to the gap. In addition, the principal stress contour exhibits a clear tension and compression field in the web region. The tension and the compression field generally initiated from the top corner of the web close to the gap with an orientation around 45 degree inclination from the vertical direction. These observations imply that much force was transferred to the top corner of the web from the top flange, and hence the web panels in the vicinity of the connection developed a tension or compression field action to resist that force. This observation was also echoed by the test phenomena as shown in Fig. 14a. In particular, evident lateral deflections of the web panel as a clear indication of a compressive zone was detected in the test, and the deformation of specimen P3-2 at the drift of 0.028 rad is obvious. In the re-test of the connection (i.e. specimen P1-2), a 6 mm thick rectangular strengthening steel plate (200 mm × 180 mm) was welded to the web to postpone buckling (Fig. 15). The web lateral deformation of specimen

P1-2 with reinforcing plates at the drift of 0.028 rad is also shown in Fig. 14b, and the lateral deflection of the web panel in the specimen P1-2 was much less evident. In general, the FE results and test evidence mentioned above suggested that significant force was transferred to the web panel near the gap, and special care is needed to suppress the premature buckling of the web before the angles developed adequate inelastic deformations. The use of strengthening plates in the web region appeared to be a promising solution to offer additional web resistance, as verified by the test evidence.

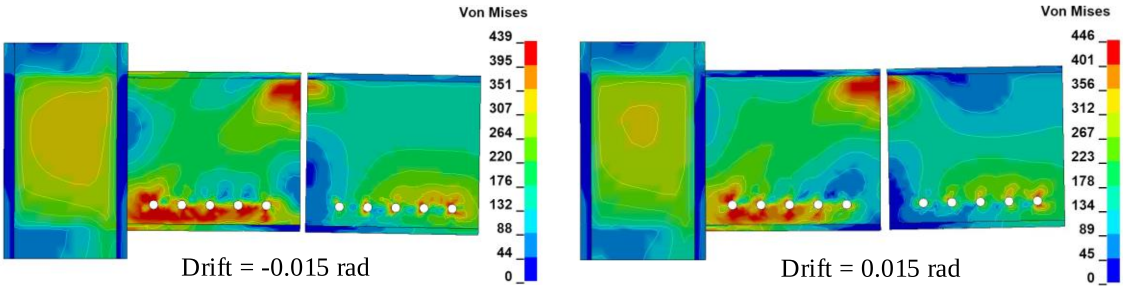

(a) Hogging

(b) Sagging

Fig. 12 Stress (von Mises stress) contour

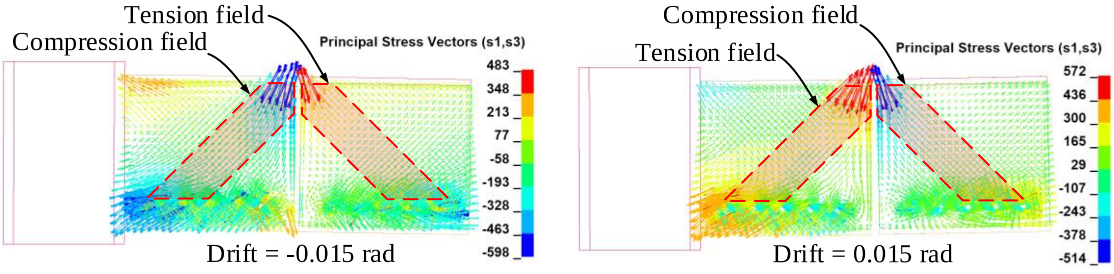

(a) Hogging

(b) Sagging

Fig. 13 Principal stress vectors contour

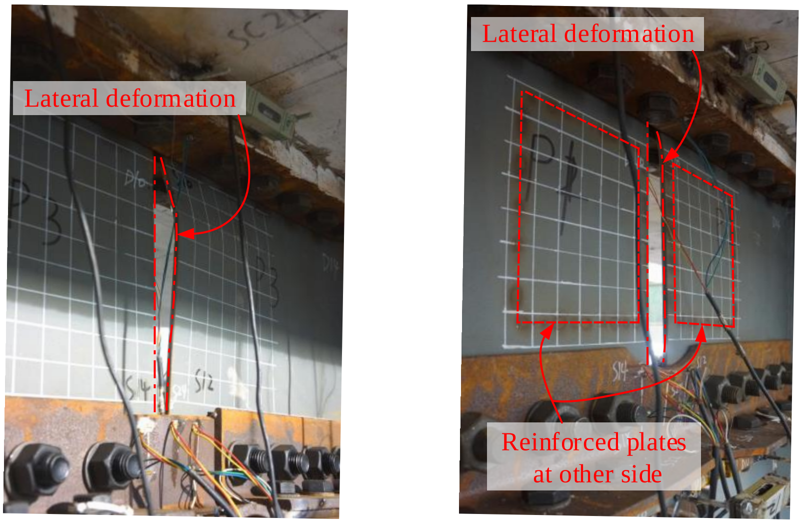

(a) P3-2 (b) P1-2

Fig. 14 Web deflection at 0.028 rad

Fig. 15 Reinforced web in specimen P1

According to force equilibrium, it may be further confirmed that the shear force close to the gap was resisted by the vertical component force of the tension or compression field which was formed in the web panel. Thus, it can also be confirmed that the shear force between the two beam segments was resisted by the elements across the gap according to the force equilibrium. Hence, it may be of great importance to reveal the shear transfer mechanism over the critical section in the gap towards a rational design in practice.

It may not be able to accurately measure the shear forces in the individual elements in the test programme. The validated FE models can be used as a reliable complementary investigation. Fig. 16 gives the shear forces percentage of connection plates, angles, and concrete slab at the critical section (Fig. 5) under various drifts. It demonstrates that the shear force was primarily taken by angles and slab initially, whereas it decreased with increasing drifts. Conversely, the connection plates took much less shear forces at small drift levels, but they became the primary source of shear resistance at large drift levels.

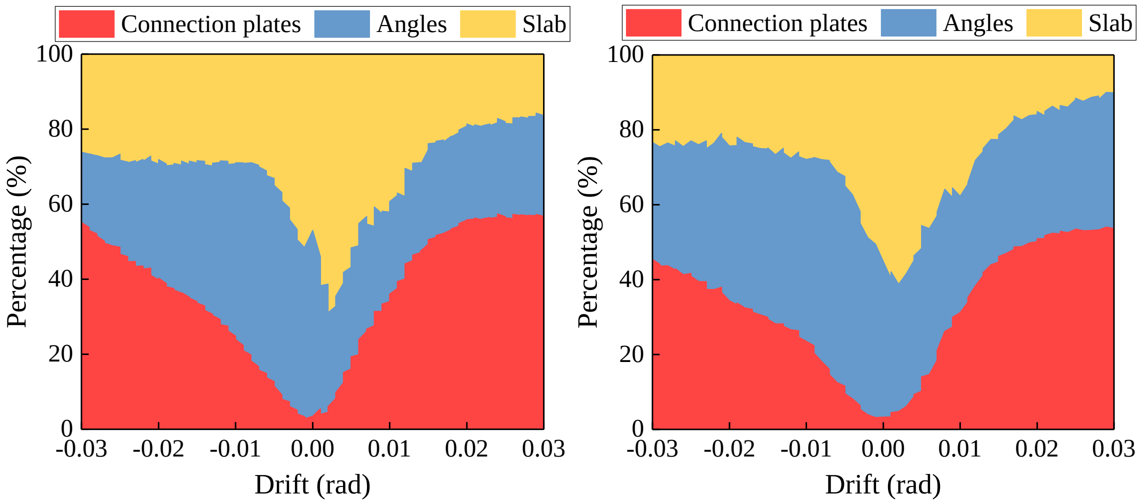

(a) P1-2 (b) P2-2

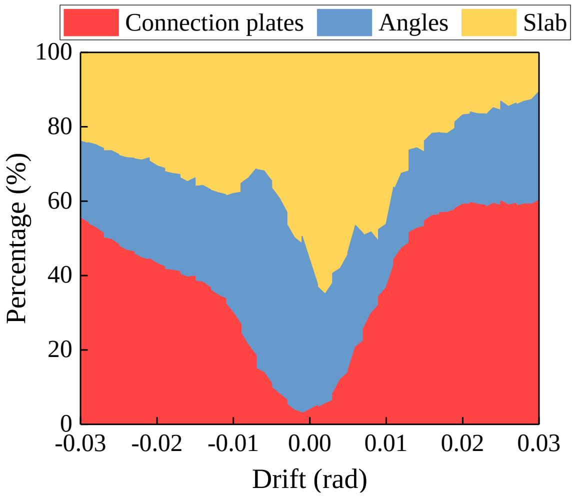

(c) P3-2

Fig. 16 Shear force distribution at the gap

The reason for this phenomenon may be summarised as follows: at the initial stage, both angles and connection plates were deformed in the elastic range, and much shear force was mobilised to angles with a higher shear stiffness. With further increase of displacement, angles were deformed into the inelastic stage with an evident decrease in shear stiffness. In contrast, the connection plates stayed elastic for a wider deformation spectrum, and hence the shear stiffness of the connection plates generally remained constant. Consequently, the connection plates dominated the shear resistance at large drifts levels. As expected, the shear force taken by the concrete slab was also decreased with increasing drift due to the shear stiffness reduction at large drift levels. In summary, the connection plates took a significant role in shear transfer at the critical section in the inelastic stage.

It is also important to note that the shear resistance of the connection plates was appreciably affected by their boundary conditions. In particular, the free deformable length of the connection plates may be idealised by a beam model with simplified boundary conditions as shown in Fig. 17. Specifically, the beam was fixed at one end and a rotational spring support at another end. In addition, a roller support may be used to simulate the bracing of the top flange. Based on the boundary conditions of the beam model, the general trend of the moment and shear diagram of the idealised beam representing the connection plates of the connection under hogging loading are shown in Fig. 17. To provide support for the aforementioned hypothesis, the moment and shear diagram of the free deformable length of the upper and lower connection plates of specimen P1-1 at the drift of 0.005 rad (in the elastic stage) was extracted from the FE database, as shown in Fig. 18. As can be seen, the general trend of the moment and shear distribution over the free deformable length of the connection plates was generally in line with the moment and shear diagram of the beam model. Note that the value of the ordinate axis was normalised by their maximum absolute value, and the length *s* and *g* in the abscissa axis are illustrated in Fig. 2b and Fig. 2c.

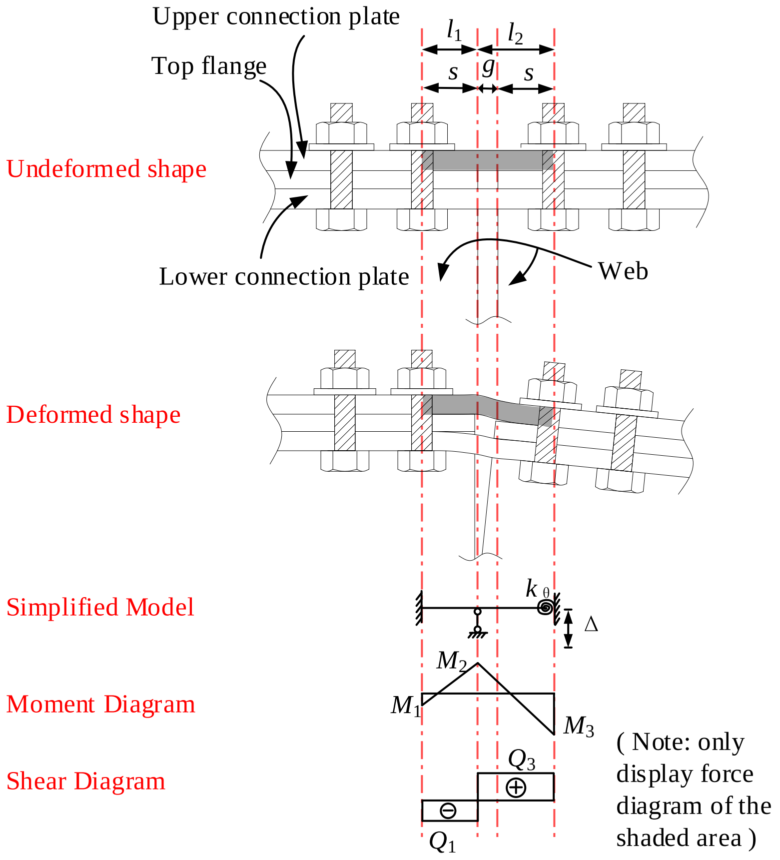

Fig. 17 Shear resistance model of the upper connection plate

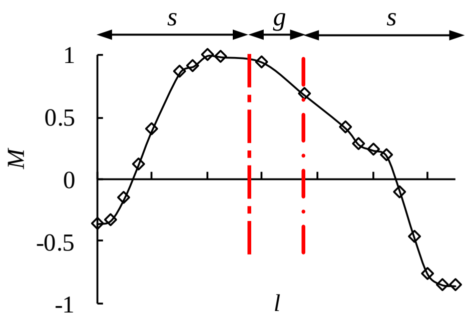

(a) Moment diagram of the upper connection plate

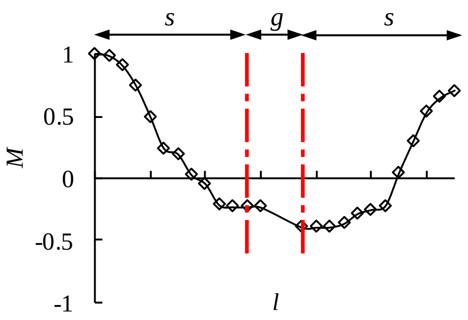

(b) Moment diagram of the lower connection plates

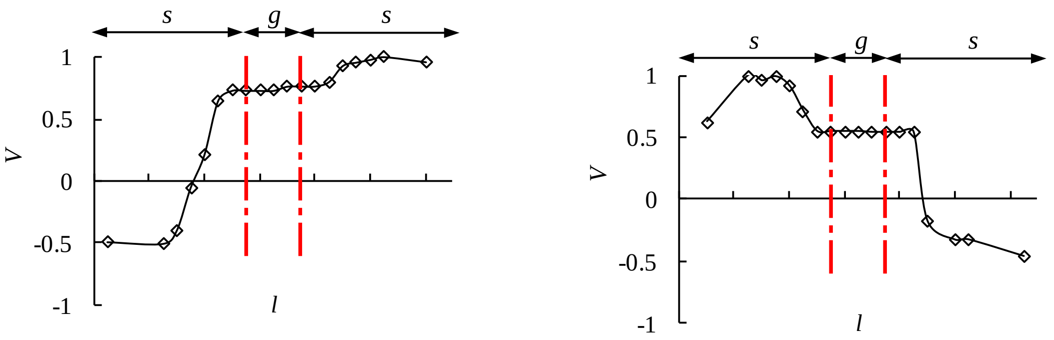

(c) Shear diagram of the upper connection plate

(d) Shear diagram of the lower connection plate

Fig. 18 Force diagram of the connection plates in specimen P1-1

Therefore, based on the experimental investigation and numerical investigation, the force transfer mechanism of the connection may be clarified. At the critical section in the gap, the moment is mainly resisted by axial forces of the angles at the bottom flange. Concurrently, the shear is mainly resisted by the angles and slab in the initial loading stage. With further development of inelastic deformation of angles, the connection plates dominate the shear resistance. Outside the gap, the shear is mobilised through the web by the vertical component of the tension or compression field. The detailed design considerations for the connection resistance will be discussed in the later section.

## 4 Design considerations

### *4.1 Moment resistance*

Fig. 19 illustrates the free body diaphragm of the connection subjected to the hogging moment, where $N_t$, $V_t$ and $M_t$, are the resultant axial force, shear force, and moment from elements at the top flange region (i.e. connection plates, and reinforced concrete slab), respectively; $N_b$, $V_b$, and $M_b$ are the resultant axial force, resultant shear, resultant moment from elements at the bottom flange (i.e. the two bottom angles), respectively. In the figure, $F$ is the applied load, $d_0$ is the distance between the force components of the force couple, and $L_f$ is the distance between the critical section and free beam end.

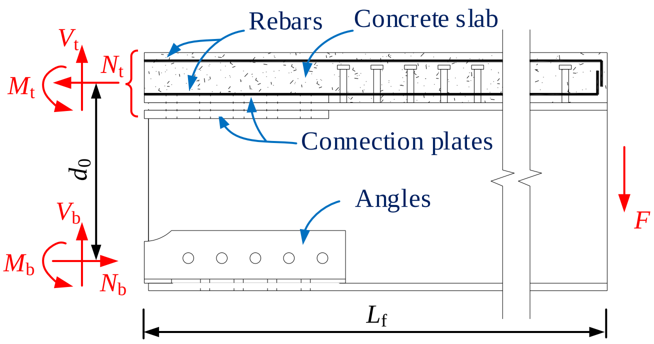

Fig. 19 Free body force diagram

According to the force and moment equilibrium, the following equations can be obtained.

$$N_t + N_b = 0 \quad (1)$$

$$V_t + V_b = F \quad (2)$$

$$M_t + M_b + N_b \cdot d_0 = F \cdot L_f \quad (3)$$

Eq. (3) demonstrates the moment equilibrium at the critical section in the gap. The total moment includes three components: a force couple resulting from the resultant force at the top and bottom elements, and the moment resistance provided by individual elements (connection plates, angles, and concrete slab). As confirmed from the test database (Fig. 8), the moment taken by the individual elements (i.e. $M_t$ and $M_b$) is much less than the force couple. Therefore, it is reasonable to ignore the moment taken by the individual elements for estimation of the connection moment resistance from a conservative perspective, and the moment equilibrium equation may be simplified by

$$N_b \cdot d_0 = F \cdot L_f \qquad (4)$$

Based on the plane section remains plane assumption, $d_0$ can be calculated with the force equilibrium equation at the critical section by discretizing each element (i.e., the top rebar, the bottom rebar, the upper connection plate, the lower connection plates, angles, and concrete slab) into a fiber [30]. Note that the contribution of concrete slab is not included under hogging condition. For the test connections, the calculated $d_0$ is 451 mm and 424 mm for sagging and hogging direction respectively. The distance $L_f$ between the loading tip and the critical section is 2025 mm. According to Eq. (4), $F/N_b$ is 0.223 and 0.209 for sagging and hogging direction respectively. Table 3 lists the $F/N_b$ values in the test (also illustrated in Fig. 7), which agree well with the calculated values by the simplified equation mentioned above. Therefore, the accuracy of Eq. (4) can be justified. The test value of $F/N_b$ in specimen P2 was much less compared to the other specimens. This phenomenon could be due to the inaccurate strain readings in the angles, as $N_b$ was calculated based on the strain readings.

Table 3. Ratio of the applied load to the axial force of angles

| Specimen | Loading direction | $F/N_b$ | | Error(%) |
|---|---|---|---|---|
| | | Test | Eq.(4) | |
| P1 | Sagging | 0.243 | 0.223 | -8.2 |
| | Hogging | 0.213 | 0.209 | -1.9 |
| P2 | Sagging | 0.164 | 0.223 | 36.0 |
| | Hogging | 0.185 | 0.209 | 13.0 |
| P3 | Sagging | 0.205 | 0.223 | 8.8 |
| | Hogging | 0.213 | 0.209 | -1.9 |

In practical cases, the angles are expected as fuses in the connection and are expected to yield before other components. Thus, the yield moment of the connection was achieved when inelastic deformation of the angles was triggered, which is determined by the axial resistance of the two angles, i.e. $N_b$, as indicated by Eq. (4). The axial resistance $N_b$ is computed as follows:

For angles subjected to tension:

$$N_b = f_y A \tag{5}$$

For angles subjected to compression:

$$N_b = \varphi f_y A \tag{6}$$

where $f_y$ = yield stress of the angles, $A$ = gross cross-sectional area of the two angles, $\varphi$ = stability factor for strength reduction due to buckling of the angles. The value of $\varphi$ can be obtained from design handbook in accordance with the slenderness ratio, the yield strength and the classification of sections, and the angles' buckling mode in Standard for design of steel structures [38]. In the specific fuse connection, the slenderness ratio of the angles is needed to obtain the compression resistance firstly. Local buckling of the angle legs may be suppressed by appropriately limiting the width-to-thickness ratio of the angle legs according to the reference [38].

### *4.1.1 Compression resistance of a single angle*

In this study, an unequal-leg angle was used, as schematically shown in Fig. 20. In the figure, point *C* is the centroid of the section. *x*-*x* and *y*-*y* are the principal axes of centroid respectively.

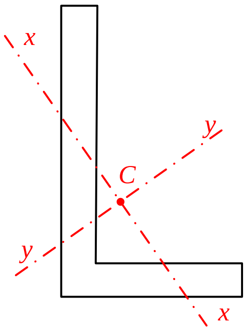

Fig. 20 Unequal-leg angle

For an unequal-leg angle, the failure may be dominated by flexural-torsional buckling. Chen [39] has proposed the following simplified equations of the equivalent slenderness ratio for calculating the inelasticity buckling resistance of an unequal-leg angle,

$$\lambda_{\mathrm{yz}} = \begin{cases} \lambda_{\mathrm{x}}\left[1+0.25\left(\lambda_{\mathrm{zi}}/\lambda_{\mathrm{x}}\right)^2\right] & \left(\lambda_{\mathrm{x}} \geq \lambda_{\mathrm{zi}}\right) \\ \lambda_{\mathrm{zi}}\left[1+0.25\left(\lambda_{\mathrm{x}}/\lambda_{\mathrm{zi}}\right)^2\right] & \left(\lambda_{\mathrm{x}} < \lambda_{\mathrm{zi}}\right) \end{cases} \tag{7}$$

$$\lambda_{\mathrm{zi}}^2 = \tau\lambda_{\mathrm{z}}^2 \tag{8}$$

$$\tau = \lambda_{\mathrm{n}}^2\left(1-0.21\lambda_{\mathrm{n}}^2\right) \tag{9}$$

$$\lambda_{\mathrm{n}} = \frac{\lambda_{\mathrm{x}}}{\pi}\sqrt{\frac{f_{\mathrm{y}}}{E}} \tag{10}$$

$$\lambda_{\mathrm{z}}^2 = \frac{\pi^2 E A i_0^2}{G I_{\mathrm{t}}} \tag{11}$$

where $\lambda_{\mathrm{yz}}$ = equivalent slenderness ratio for the unequal-leg angle, $i_0$ = polar radius of gyration about the shear centre, $\lambda_{\mathrm{x}}$ = slenderness ratio about the major principal axis, $\lambda_{\mathrm{z}}$ = equivalent slenderness ratio for torsional buckling, and $I_{\mathrm{t}}$ = torsional constant of the single angle section.

The slenderness ratio for a single angle can be determined by Eq. (7), and the stability factor for a single angle may be correspondingly computed [38].

### *4.1.2 Compression resistance of double angles*

Fig. 21 shows the double-angle section. In the figure, point *C* and point *S* are the centroid of the section and the shear centre of the section, respectively. *x*-axis and *y*-axis are the principal axes.

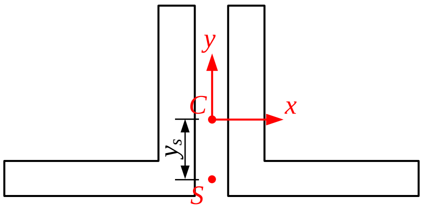

Fig. 21 Double-angle compound section

As a member of monosymmetric section, the double-angle section has two possible buckling modes: flexural buckling about the non-symmetric axis (*x*-axis in Fig. 21) and flexural-torsional buckling about the symmetric axis (*y*-axis in Fig. 21). For flexural buckling, the slenderness ratio $\lambda_x'$ is calculated by Eq. (12) based on the sectional parameters of the double-angle section.

$$\lambda_x' = \frac{l_x}{i_x} \tag{12}$$

where $l_x$ = effective length about the *x*-axis and $i_x$ = radius of gyration of the double-angle section about *x*-axis.

For flexural-torsional buckling, the flexural-torsional slenderness ratio is calculated by following equations [38],

$$\lambda_{yz}' = \sqrt{\frac{\lambda_y'^2 + \lambda_z'^2 + \sqrt{\left(\lambda_y'^2 + \lambda_z'^2\right)^2 - 4\lambda_y'^2 \lambda_z'^2 \left(1 - y_s^2 / i_0^2\right)}}{2}} \tag{13}$$

$$\lambda_{z}^{'2}=\frac{Ai_{0}^{2}}{{I_{w}}/{l_{w}^{2}}+{GI_{t}}/{\pi^{2}E}} \tag{14}$$

where $\lambda_{yz}'$ = torsional slenderness ratio of the double-angle section, $\lambda_{y}'$ = slenderness ratio about the $y$-axis of the double-angle section, $\lambda_{z}'$ = equivalent slenderness ratio for torsional buckling, $y_s$ = distance between centroid and shear centre of the double-angle section, $i_0$ = polar radius of gyration about the shear centre of the double-angle section, $I_w$ = sectorial moment of inertia of the double-angle section and $l_w$ = effective length for torsional buckling.

With the greater value of $\lambda_{x}'$ and $\lambda_{yz}'$, the stability factor for the double-angle component can be obtained by [38] as well.

Therefore, the final stability factor in Eq. (6) should be the minimum of $\varphi_1$ and $\varphi_2$, where $\varphi_1$ and $\varphi_2$ are the stability factors of single-angle component and double-angle component, respectively.

The calculated stability factors of the angles in the test are listed in Table 4.

Table 4. Stability factor

| Specimen | $\varphi_1$ | $\varphi_2$ | $\varphi = \min(\varphi_1, \varphi_2)$ |
|---|---|---|---|
| P1, P3 | 0.994 | 0.992 | 0.992 |
| P2 | 0.998 | 0.997 | 0.997 |

The applied force corresponding to yielding of the angles of the test specimens was calculated according to Eq. (15), and the results are indicated by “$F_y$” in Fig. 10.

$$F_{y}=\frac{N_{b}d_{0}}{L_{f}} \tag{15}$$

It can be seen that the design equations may be used to predict the yield moment of the connection with satisfactory accuracy. In pursuit of energy dissipation of the connection, a stocky section of angles may be used to avoid severe strength reduction induced by buckling.

### *4.2 Shear resistance*

According to the FE results of the connections, it may be confirmed that the shear force at the critical section is resisted by angles, concrete slab, and connection plates in the initial loading stage. Recalling that the shear force propagation of the connection was varied with connection deformations, it may be conservative to ignore the contribution of angles and the concrete slab to the connection shear resistance. Thus, the design shear resistance of the connection may be quantified by the connection plates. Fig. 17 shows the deformed shape of the connection plates and the simplified beam model.

Based on the force and moment equilibrium principle, the moment and shear force in Fig. 17 can be computed as follows:

$$M_1 = -\frac{6EI}{l_2} \cdot \frac{1+c}{(3+c)l_1 + 4l_2} \cdot \Delta \tag{16}$$

$$M_2 = \frac{12EI}{l_2} \cdot \frac{1+c}{(3+c)l_1 + 4l_2} \cdot \Delta \tag{17}$$

$$M_3 = -\frac{12EI}{l_2^2} \cdot \frac{(l_1 + 2l_2)c}{(3+c)l_1 + 4l_2} \cdot \Delta \tag{18}$$

$$Q_1 = \frac{18EI}{l_1 l_2} \cdot \frac{1+c}{(3+c)l_1 + 4l_2} \tag{19}$$

$$Q_2 = \frac{6EI}{l_1 l_2^3} \cdot \frac{3l_2^2\left(1+c\right) + 2l_1^2 c + 2l_1 l_2\left(1+3c\right)}{\left(3+c\right)l_1 + 4l_2} \cdot \Delta \tag{20}$$

$$Q_3 = \frac{12EI}{l_2^3} \cdot \frac{l_1 c + l_2(1+3c)}{(3+c)l_1 + 4l_2} \cdot \Delta \tag{21}$$

$$c = \frac{1}{1+\frac{4EI}{k_\theta l_2}} \tag{22}$$

where $E$ = steel modulus, $I$ = moment of inertia of the studied connection plate, $l_1$ = end distance from the centreline of innermost bolts to the edge of the gap ($s$ in Fig. 2a and Fig. 17), $l_2$ = summation of the end distance and the gap width (i.e. $s+g$ in Fig. 2a and Fig. 17), $\Delta$ = lateral displacement at the two ends, $c$ = boundary constant depending on the spring constant $k_\theta$. When the boundary condition at the right side of the beam is a pinned support (i.e. $k_\theta = 0$), $c = 0$; in cases of a fixed end (i.e. $k_\theta = \infty$), $c = 1$.

On the other hand, $Q_1$ and $Q_3$ are the reaction forces from the bolt, whereas $Q_2$ is the reaction force applied by the top flange at the gap edge. Note that $Q_3$ is the shear force of the connection plate at the gap as shown in the shear diagram of Fig. 17. In this context, the shear resistance of the connection can be determined once the moment of the governing sections reach their yield moment $M_{\mathrm{y,plate}}$,

$$M_{\mathrm{y,plate}} = \max\left(M_1, M_2, M_3\right) \tag{23}$$

Substituting Eq. (23) into Eq. (16)-(21), the shear resistance of the studied connection plates is given by

$$Q_{\mathrm{y}} = \begin{cases} \dfrac{\left(a_1+3\right)c+1}{1+c} \cdot \dfrac{M_{\mathrm{y,plate}}}{l_2} & \left(0 \le c \le c_0\right) \\ \dfrac{\left(a_1+3\right)c+1}{\left(a_1+2\right)c} \cdot \dfrac{M_{\mathrm{y,plate}}}{l_2} & \left(c_0 < c \le 1\right) \end{cases} \tag{24}$$

$$a_1 = \frac{l_1}{l_2} \tag{25}$$

$$c_0 = \frac{l_2}{l_1 + l_2} \tag{26}$$

Afterwards, the total shear resistance of the fuse connection, $F_{\mathrm{v}}$, shall be taken as the summation of the shear resistance of the upper connection plate and lower connection plates,

$$F_{\mathrm{v}} = \sum Q_{\mathrm{y}} \tag{27}$$

where $Q_{\mathrm{y}}$ is the shear resistance of a connection plate, calculated by Eq. (24).

Note that the shear resistance $Q_{\mathrm{y}}$ is a piecewise function depending on the boundary conditions of the beam model (i.e. $c$). For simplification, the influence of the fuse connection on the flexural stiffness of the composite beam may be neglected, which is a feasible idealisation as confirmed in the literature [30]. Thus, the value of $c$ can be estimated by assuming that the vertical translation ($\Delta_{\mathrm{A}}$ and $\Delta_{\mathrm{B}}$) and rotation ($\theta_{\mathrm{A}}$ and $\theta_{\mathrm{B}}$) at both ends of the free deformable length of the connection plate are equal to that at the same location in a continuous composite beam (point A and B in Fig. 22). The relative vertical displacement $\Delta$ and rotation $\theta$ of the two ends is then given by

$$\Delta = \Delta_{\mathrm{B}} - \Delta_{\mathrm{A}} = \frac{F}{6EI_{\mathrm{b}}}\left[2L(L_1+L_2)^2 + (L_1+L_2)^2 L_3 - 2LL_1^2 - L_1^2(L_1+L_2)\right] \tag{28}$$

$$\theta = \theta_{\mathrm{B}} - \theta_{\mathrm{A}} = \frac{F}{2EI_{\mathrm{b}}}\left[(L_1+L_2)(L+L_3) - L_1(L+L_2+L_3)\right] \tag{29}$$

where $\Delta_{\mathrm{A}}$ = the absolute vertical displacement at point A, $\theta_{\mathrm{A}}$ = the absolute rotation at point A, $\Delta_{\mathrm{B}}$ = the absolute vertical displacement at the point B, $\theta_{\mathrm{B}}$ = the absolute rotation at point B, $F$ = the applied load at the beam tip, $L_1 = a + g/2$, $L_2 = l_1 + l_2$, $L_3 = L - L_1 - L_2$, $L$ = the total length of the composite beam, $a$ = the location of the critical section (Fig. 1), $g$ = the gap width (Fig. 1), $I_{\mathrm{b}}$ = the moment of inertia of the composite beam.

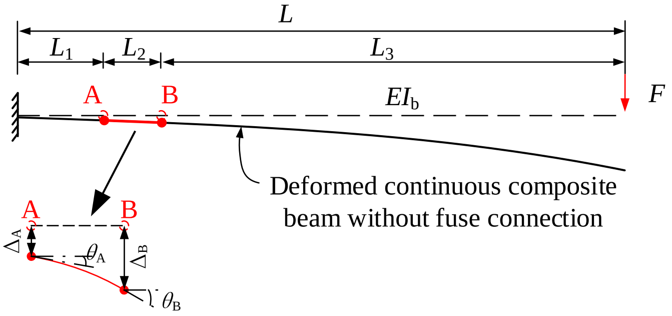

Fig. 22 Analytical model

The rotation stiffness of the spring, $k_\theta$, can be determined by,

$$k_\theta = |M_3| / \theta \tag{30}$$

where $\theta$ is the absolute rotation of the spring, determined by Eq. (29) and $M_3$ is the moment of the spring, can be calculated by Eq. (18).

Combining Eq. (18), Eq. (22), Eq. (28), Eq. (29), and Eq. (30), $c$ may be re-arranged as follows:

$$c = \frac{3(l_1 + 2l_2) - (3l_1 l_2 + 4l_2^2) \cdot \dfrac{\theta}{\Delta}}{\dfrac{\theta}{\Delta} \cdot l_1 l_2 + 3(l_1 + 2l_2)} \tag{31}$$

where $l_1$ = end distance from centreline of innermost bolts to the edge of the gap ($s$ in Fig. 2a), $l_2$ = summation of the end distance and the gap width (i.e. $s$+$g$ in Fig. 2a), $\Delta$, $\theta$ = the relative vertical displacement and rotation of the two ends, which can be calculated by Eq. (28) and Eq. (29), respectively.

The calculated value of $c$ by Eq. (31) is 0.89 based on the test connections, and thereby obtaining the computed shear resistance $F_v$ by Eq. (24), as also shown in Fig. 10. The design shear resistance $F_v$ is higher than the force corresponding to yield moment resistance $F_y$. These results showed that the connection plates had enough shear resistance and thus deformed in the elastic range, which was in accordance with strain readings of the connection plates in the tests [30].

## 5 Conclusions

As a continuation of the previous experimental programme, this paper took further insights into the force transfer mechanism and the corresponding design considerations of a novel composite connection equipped with angle fuse elements arranged at the bottom of the steel beam. The force/moment evolution of three full-scale test connections was examined in detail. Then, detailed finite element models of the test connections were developed, and the adequacy of the FE modelling techniques was justified by the test responses. Based on the verified FE models, the stress distribution and force transfer mechanism of the connection were explored. The load-carrying behaviour of the connection from the initial loading stage to the deformation with evident inelasticity was investigated, and the force evolution of the individual elements in the connection was clarified.

According to the experimental and numerical study, it was observed that the moment at the connection was resisted by a force couple produced by the resultant axial forces from the connection plates, reinforced concrete slab, and bottom angles. The shear at the section of the gap is resisted by connection plates, angles, and concrete slab. The shear percentage ratio of each element is varied with the deformation: the majority of the shear is taken by angles and slab initially, whereas the connection plates dominate the shear resistance as inelasticity is developed in angles and the slab. It was also observed that a compression field may be formed in the web panel, and special caution may need to be exercised to prevent early local buckling of the web.

Based on the force transfer mechanism of the connection, a simplified beam model for quantifying the shear resistance of the connection plates was established. The design equations of the moment resistance of the connection governed by yielding of the angle fuse elements were proposed. The comparison between the test responses and design predictions confirmed the sufficiency of the ability of the proposed equations for quantifying the moment resistance of the connection. In addition, the design equations of the shear resistance of the connection based on the beam model of the connection plates were also developed.

## Acknowledgement

This work is supported by National Natural Science Foundation of China under Grant No. 51578403, 51890902 and 51708197. Partial funding support from Chinese National Engineering Research Centre for Steel Construction, The Hong Kong Polytechnic University (Project No. 1-BBV4) was gratefully acknowledged. The corresponding author would like to thank the constant support from his beloved wife Siqin, his daughter Yutong and all his family members, particularly in this hard period.

## References

[1] Uang C M, Yu Q S K, Noel S, Gross J. Cyclic testing of steel moment connections rehabilitated with RBS or welded haunch. J Struct Eng 2000; 126(1): 57-68.

[2] Jones S L, Fry G T, Engelhardt M D. Experimental evaluation of cyclically loaded reduced beam section moment connections. J Struct Eng 2002; 128(4): 441-451.

[3] Chambers J J, Almudhafar S, Stenger F. Effect of reduced beam section frame elements on stiffness of moment frames. J Struct Eng 2003; 129(3): 383-393.

[4] Kim T, Whittaker A S, Gilani A S J, Bertero V V. Cover-plate and flange-plate steel moment-resisting connections. J Struct Eng 2002; 128(4): 474-482.

[5] Kim T, Whittaker A S, Gilani A S J, Bertero V V, Takhirov S M. Experimental evaluation of plate-reinforced steel moment-resisting connections. J Struct Eng 2002; 128(4): 483-491.

[6] Jazany R A, Ghobadi M S. Seismic evaluation and upgrading details of plate-reinforced moment-resisting connections. J Constr Steel Res 2018; 150: 230-248.

[7] Ricles J M, Sause R, Garlock M M, Zhao C. Posttensioned seismic-resistant connections for steel frames. J Struct Eng 2001; 127(2): 113-121.

[8] Rojas P, Ricles J M, Sause R. Seismic performance of post-tensioned steel moment resisting frames with friction devices. J Struct Eng 2005; 131(4): 529-540.

[9] Saffari H, Hedayat A A, Nejad M P. Post-Northridge connections with slit dampers to enhance strength and ductility. J Constr Steel Res 2013; 80: 138-152.

[10] Oh S H, Kim Y J, Ryu H S. Seismic performance of steel structures with slit dampers. Eng Struct 2009; 31(9): 1997-2008.

[11] Calado L, Proença J M, Espinha M, Castiglioni C A. Hysteretic behaviour of dissipative bolted fuses for earthquake resistant steel frames. J Constr Steel Res 2013; 85: 151-162.

[12] Shen Y, Christopoulos C, Mansour N, Tremblay R. Seismic design and performance of steel moment-resisting frames with nonlinear replaceable links. J Struct Eng 2011;

137(10): 1107-1117.

[13] Jiang Z, Dou C, Zhang A, Wang Q, Wu Y. Experimental study on earthquake-resilient prefabricated cross joints with L-shaped plates. Eng Struct 2019; 184: 74-84.

[14] Jiang Z, Yang X F, Dou C, Li C, Zhang A. Cyclic testing of replaceable damper: Earthquake-resilient prefabricated column-flange beam-column joint. Eng struct 2019; 183: 922-936.

[15] Zhang A, Jiang Z, Li C, Liu X. Low cycle reciprocating tests of earthquake-resilient prefabricated column-flange beam-column joints with different connection forms. J Constr Steel Res 2020; 163:105771

[16] Mahmoudi F, Dolatshahi K M, Mahsuli M, Nikoukalam M T. Experimental study of steel moment resisting frames with shear link. J Constr Steel Res 2019; 154: 197-208.

[17] Nikoukalam M T, Dolatshahi K M. Development of structural shear fuse in moment resisting frames. J Constr Steel Res 2015; 114: 349-361.

[18] Jiang Z Q, Dou C, Zhang H, Wang Q, Yang Y H. Experimental study of earthquake-resilient prefabricated beam-column steel joint with L-shaped plate. J Constr Steel Res 2020; 166: 105928.

[19] Köken A, Köroğlu M A. Experimental study on beam-to-column connections of steel frame structures with steel slit dampers. J Perform Constr Fac 2015; 29(2): 04014066.

[20] Wolski M, Ricles J M, Sause R. Experimental study of a self-centering beam-column connection with bottom flange friction device. J Struct Eng 2009; 135(5): 479-488.

[21] Rad A A, MacRae G A, Hazaveh N K, Ma Q. Shake table testing of a low damage steel building with asymmetric friction connections (AFC). J Constr Steel Res 2019; 155:

129-143.

[22] Kim H J, Christopoulos C. Friction damped posttensioned self-centering steel moment-resisting frames. J Struct Eng 2008; 134(11): 1768-1779.

[23] Mander T J, Rodgers G W, Chase J G, Mander J B, MacRae G A, Dhakal R P. Damage avoidance design steel beam-column moment connection using high-force-to-volume dissipators. J Struct Eng 2009; 135(11): 1390-1397.

[24] Feng W, Fang C, Wang W. Behavior and design of top flange-rotated self-centering steel connections equipped with SMA ring spring dampers. J Constr Steel Res 2019; 159: 315-329.

[25] Garlock M E M, Li J. Steel self-centering moment frames with collector beam floor diaphragms.J Constr Steel Res 2008; 64(5): 526-538.

[26] Fang C, Wang W, He C, Chen Y. Self-centring behaviour of steel and steel-concrete composite connections equipped with NiTi SMA bolts. Eng Struct 2017; 150: 390-408.

[27] Nakashima M, Matsumiya T, Suita K, Zhou F. Full-scale test of composite frame under large cyclic loading. J Struct Eng 2007; 133(2): 297-304.

[28] Liu J, Astaneh-Asl A. Cyclic testing of simple connections including effects of slab. J Struct Eng 2000; 126(1): 32-39.

[29] Nie J, Huang Y, Fan J. Experimental study on load-bearing behavior of rectangular CFST frame considering composite action of floor slab. J Build Struct 2011; 32(3): 99-108. (in Chinese)

[30] He X, Chen Y, Eatherton M R, Shao T. Experimental evaluation of replaceable energy dissipation connection for moment-resisting composite steel frames. J Struct Eng

2018; 144(6): 04018042.

[31] Tahmasebinia F, Ranzi G, Zona A. Probabilistic three-dimensional finite element study on composite beams with steel trapezoidal decking. J Constr Steel Res 2013; 80: 394-411.

[32] Ataei A, Moradi M, Valipour H R, Bradford M A. Finite element modelling of demountable precast reinforced concrete deck slabs with external confining system. J Constr Steel Res 2018; 151: 204-215.

[33] Tahmasebinia F, Ranzi G, Zona A. Beam tests of composite steel-concrete members: a three-dimensional finite element model. International J Steel Struct 2012; 12(1): 37-45.

[34] Queiroz F D, Vellasco P C G S, Nethercot D A. Finite element modelling of composite beams with full and partial shear connection. J Constr Steel Res 2007; 63: 505-521.

[35] Baskar K, Shanmugam N E, Thevendran V. Finite-Element Analysis of Steel–Concrete Composite Plate Girder. J Struct Eng 2002; 128(9): 1158-1168.

[36] Hallquist J O. LS-DYNA theory manual, Livemore Software Technology Corporation 2006.

[37] Moharrami M, Koutromanos I. Triaxial constitutive model for concrete under cyclic loading. J Struct Eng 2016; 142(7): 04016039.

[38] GB50017-2017. Standard for design of steel structures (GB50017-2017). China Architecture and Building Press, Beijing, China; 2017.

[39] Chen S. Elastic and inelastic stability capacity of single angle under axial compression. J Build Struct 2012; 33(10): 134-141. (in Chinese)

**Declaration of interests**

☒ The authors declare that they have no known competing financial interests or personal relationships that could have appeared to influence the work reported in this paper.

☐The authors declare the following financial interests/personal relationships which may be considered as potential competing interests:

# Author statement

Xiuzhang He**:** Conceptualization, Writing-Original draft preparation, Validation, Formal analysis, Methodology, Software

Ke Ke***:** Conceptualization, Writing-Reviewing and Editing, Funding acquisition

Lihua Guo**:** Visualization, Formal analysis, Software

Michael CH Yam**:** Resources, Writing-Reviewing and Editing

Zhihui Wang**:** Visualization, Formal analysis, Software